



## Article

# Lattice Defects Engineering in W-, Zr-doped BiVO<sub>4</sub> by Flame Spray Pyrolysis: Enhancing Photocatalytic O<sub>2</sub> Evolution

Panagiota Stathi, Maria Solakidou and Yiannis Deligiannakis \*

Laboratory of Physics Chemistry of Materials & Environment, Department of Physics, University of Ioannina, 45110 Ioannina, Greece; pstathi@cc.uoi.gr (P.S.); maria-sol@windowslive.com (M.S.)

\* Correspondence: ideligia@uoi.gr

**Abstract:** A flame spray pyrolysis (FSP) method has been developed, for controlled doping of BiVO<sub>4</sub> nanoparticles with W and Zr *in tandem* with the oxygen vacancies (Vo) of the BiVO<sub>4</sub> lattice. Based on XPS and Raman data, we show that the nanolattice of W-BiVO<sub>4</sub> and Zr-BiVO<sub>4</sub> can be controlled to achieve optimal O<sub>2</sub> evolution from H<sub>2</sub>O photocatalysis. A synergistic effect is found between the W- and Zr-doping level in correlation with the Vo-concentration. FSP- made W-BiVO<sub>4</sub> show optimal photocatalytic O<sub>2</sub>-production from H<sub>2</sub>O, up to 1020 μmol/(g × h) for 5%W-BiVO<sub>4</sub>, while the best performing Zr-doped achieved 970 μmol/(g × h) for 5%Zr-BiVO<sub>4</sub>. Higher W- or Zr-doping resulted in deterioration in photocatalytic O<sub>2</sub>-production from H<sub>2</sub>O. Thus, engineering of FSP-made BiVO<sub>4</sub> nanoparticles by precise control of the lattice and doping-level, allows significant enhancement of the photocatalytic O<sub>2</sub>-evolution efficiency. Technology-wise, the present work demonstrates that flame spray pyrolysis as an inherently scalable technology, allows precise control of the BiVO<sub>4</sub> nanolattice, to achieve significant improvement of its photocatalytic efficiency.

**Keywords:** BiVO<sub>4</sub>; W-doping; Zr-doping; flame spray pyrolysis; oxygen vacancies; defects; Raman; XPS; photocatalysis; water splitting; O<sub>2</sub>



**Citation:** Stathi, P.; Solakidou, M.; Deligiannakis, Y. Lattice Defects Engineering in W-, Zr-doped BiVO<sub>4</sub> by Flame Spray Pyrolysis: Enhancing Photocatalytic O<sub>2</sub> Evolution. *Nanomaterials* **2021**, *11*, 501. <https://doi.org/10.3390/nano11020501>

Academic Editor: Chiara Maccato  
Received: 28 December 2020  
Accepted: 7 February 2021  
Published: 16 February 2021

**Publisher's Note:** MDPI stays neutral with regard to jurisdictional claims in published maps and institutional affiliations.



**Copyright:** © 2021 by the authors. Licensee MDPI, Basel, Switzerland. This article is an open access article distributed under the terms and conditions of the Creative Commons Attribution (CC BY) license (<https://creativecommons.org/licenses/by/4.0/>).

## 1. Introduction

Since the 1972 report by Fukushima and Honda [1] on the photocatalytic water splitting using TiO<sub>2</sub>, several other types of semiconductors have been evaluated as photocatalysts. Tungstates [2], vanadates molybdates and niobates [3] have been found to be efficient photocatalysts for O<sub>2</sub> evolution from H<sub>2</sub>O. So far, among the most efficient O<sub>2</sub>-evolving photocatalysts IrO<sub>2</sub> stands-out as the best [3] however its high-cost is prohibitive. Currently O<sub>2</sub>-production efficiencies for IrO<sub>2</sub> photocatalysts are reported to be in the range 5000–7000 μmol/(g × h) [3]. TiO<sub>2</sub> as a reference material has been extensively studied for O<sub>2</sub>-evolution photocatalysis [1,3]. So far O<sub>2</sub>-production efficiencies for TiO<sub>2</sub> photocatalysts are in the range 50–200 μmol/(g × h) [4]. BiVO<sub>4</sub> is among the most promising O<sub>2</sub>-evolving photocatalysts, i.e., due to suitable narrow band-gap energy (E<sub>g</sub>), i.e., 2.2–2.4 eV and high optical adsorption efficiency. Monoclinic scheelite BiVO<sub>4</sub> is an *n*-type semiconductor with a direct band gap of 2.4 eV, thus it absorbs visible light, λ = 420–530 nm with an optical penetration depth of l<sub>p</sub> = 100–500 nm [4]. BiVO<sub>4</sub> can be used in Z-scheme photocatalysts [4], i.e., to heal low mobility of photogenerated charge carriers in BiVO<sub>4</sub> and high recombination rates of photogenerated electron-hole pairs [5].

So far, there is credible evidence that doping of BiVO<sub>4</sub> can be an efficient strategy to improve the photocatalytic performance [6–19]. Highly encouraging results show that appropriate doping of BiVO<sub>4</sub>, i.e., with Mo [7], W [8,9], P [10], B [11] or Ce [12] can result in significant enhancement of O<sub>2</sub>-evolution. Currently, all reported methods for synthesis of doped BiVO<sub>4</sub> photocatalysts, concern liquid-chemistry methods. For example Ikeda et al. [13] have synthesized Zr-doped BiVO<sub>4</sub> photocatalysts, using a coprecipitation method, and their material exhibited O<sub>2</sub> evolution 500 μmol/(g × h) [15]. A W-doped BiVO<sub>4</sub> catalyst had achieved O<sub>2</sub> production of 665 μmol/(g × h) [14]. In 2012, Lee and

coworkers [15] had compared the O<sub>2</sub>-evolution efficiency for 12 types of different metal-ion dopants in BiVO<sub>4</sub>, prepared by the same solid-state reaction process. Among the tested dopants, only W and Mo showed a dramatic enhancement of O<sub>2</sub> evolution activity, i.e., 600 μmol/(g × h) and 2000 μmol/(g × h) respectively vs. 100 μmol/(g × h) for undoped BiVO<sub>4</sub>. Cerium-doped BiVO<sub>4</sub> prepared with a solvothermal method [19] achieved O<sub>2</sub> production of 325 μmol/(g × h).

Flame spray pyrolysis (FSP) is an one-step flame-process synthesis [16], which allows engineering of nanoparticles with well-controlled composition, phase-purity, crystallinity and size [17]. Originally, FSP synthesis of BiVO<sub>4</sub> has been reported by Amal, Madder and Kudo [18]. In [18] it was found that when the FSP-made BiVO<sub>4</sub> contains excess of lattice-defects, this is detrimental for photocatalytic O<sub>2</sub> production. Thus, the authors had developed a post-FSP liquid-phase treatment [18] to optimize the photocatalytic performance of BiVO<sub>4</sub>, i.e., achieving 300 μmol/(g × h) O<sub>2</sub> per gram of BiVO<sub>4</sub> per hour. Their post-FSP protocol included aqueous acid-treatment with addition of bismuth (Bi) and vanadium (V) atoms, which was shown to promote the formation of photo catalytically active scheelite-monoclinic BiVO<sub>4</sub> phase. On the other hand, theoretical calculations [19] show that oxygen-vacancies, if appropriately engineered, can be beneficial for photocatalytic O<sub>2</sub> production. More specifically, a distinct role of surface-oxygen vacancies vs. bulk-oxygen vacancies have been dictated by DFT calculations for pure BiVO<sub>4</sub> [19]. According to Wang et al. [19], photoinduced polarons formed from O-vacancies in the bulk can contribute to conductivity, while those at the surface might have an opposite effect. Intriguingly, it has been suggested that surface O-vacancies might have a beneficial effect on O<sub>2</sub>-adsorption on BiVO<sub>4</sub> during photocatalysis, i.e., according to the theoretical study in [19]. Another theoretical study indicated that the fine-balance between surface and bulk O-vacancies should be considered carefully in the quest of optimal O<sub>2</sub> photoproduction by BiVO<sub>4</sub> [20].

The pivotal role of O-vacancies has also been reported for doped-BiVO<sub>4</sub> also. Specifically, in W-doped BiVO<sub>4</sub> [20], theoretical calculations indicate that a localized-state formed inside the band gap in W-doped BiVO<sub>4</sub> containing oxygen vacancies [20] can serve as a recombination center, thus it lowers the photoinduced charge-separation efficiency [20]. In [20] it was predicted that better performance can be achieved by introducing oxygen vacancy *on the surface* of a W-doped BiVO<sub>4</sub>, simultaneously avoiding oxygen vacancy *in the bulk* [20]. The same trend seems to be true for Mo-doped BiVO<sub>4</sub> [7]. DFT calculations indicate that surface oxygen quasi-vacancies enhance O<sub>2</sub> photoproduction in Mo-doped monoclinic BiVO<sub>4</sub> by facilitating separation of photoinduced carriers [7].

Herein, we used flame spray pyrolysis as a method to engineer W- and Zr-doped BiVO<sub>4</sub> with controlled O-vacancies' content. Using XPS and Raman spectroscopies we have studied the interrelation between W- or Zr-doping and O-vacancies, in conjunction with photocatalytic O<sub>2</sub> evolution. Thus, the main aims of the present study are: (i) the development FSP protocols for synthesis of doped-BiVO<sub>4</sub> with controlled W- and Zr-dopant content, (ii) to optimize the nanomaterials' photocatalytic O<sub>2</sub> production from H<sub>2</sub>O oxidation, and (iii) to discuss the underlying catalytic mechanism, revealing the crucial role of oxygen vacancies in conjunction with W and Zr.

## 2. Materials and Methods

All solvents used were of commercial grade and have been purchased from Sigma Aldrich. Bi and V metal-organic precursors, i.e., bismuth (III) nitrate pentahydrate (Bi(NO<sub>3</sub>)<sub>3</sub>) (99% purity) and vanadium(V) oxytriisopropoxide (OV(OCH(CH<sub>3</sub>)<sub>2</sub>)<sub>3</sub>) (99% purity) respectively. For the dopings, the W- and Zr-precursors used were ammonium metatungstate hydrate (85% purity) and zirconium (IV) isopropoxide isopropanol complex (99.9% purity) obtained from Strem Chemicals.

### 2.1. Flame Synthesis of Nanocatalysts

The lab-scale FSP reactor used for the synthesis of nanocatalysts has been described recently [21]. The bismuth precursor was prepared by dissolving Bi-nitrate in (triethylene glycol dimethyl ether/acetic acid (70/30 *v/v*)) (0.5 M) and sonicated for 30 min at 50 °C. The V-precursor was prepared by dissolving vanadium-oxytriisopropoxide in xylene (0.5 M). For the doping materials, ammonium metatungstate hydrate or zirconium (IV) isopropoxide was added in the Bi/V mixture solution at the nominal atom ratios, as specified in Table 1. To produce the particles in FSP, a 1:1 mixture of Bi:V solution was fed, atomized through a 300 µm capillary at 5 mL/L and dispersed by 5 L/min O<sub>2</sub> (Linde, purity > 99%). A self-sustained O<sub>2</sub>:CH<sub>4</sub> (5 L/min and 1.5 L/min) pilot-flame was used to initiate combustion. Pressure-drop at the nozzle tip was fixed at 2 bar, and an additional 5 L/min sheath-O<sub>2</sub> was used. The product powder was collected, using a vacuum pump (Busch V40), on a glass microfiber filter (Albet). All prepared materials studied herein, are listed in Table 1. For the sake of simplicity, in Table 1 and throughout the text, the samples were code-named according to their nominal % dopant loading, i.e., %W or % Zr in the precursor-solution, and their synthesis configuration. As shown previously [18], adjusting the particle-collection filter to higher temperatures > 340 °C promotes the in-situ formation of monoclinic scheelite BiVO<sub>4</sub> phase [18]. Accordingly, in our set-up the FSP particle-collecting filter temperature was adjusted to be 350–360 °C.

**Table 1.** Properties of the flame spray pyrolysis (FSP)-made BiVO<sub>4</sub> nanocatalysts \*.

Material	Nominal Dopant Content in the FSP Precursor (%w:w)	Dopant Content Measured by XRF	XRD Size (nm ± 0.5)	SSA (m <sup>2</sup> g <sup>-1</sup> ± 0.8)	Band-Gap Eg (eV)
BiVO <sub>4</sub>	-	-	22.1	37.7	2.36
W-Doped nanocatalysts					
0.5W-BiVO <sub>4</sub>	0.5	Not detectable	17.5	45.0	2.31
1W-BiVO <sub>4</sub>	1	0.6	19.8	46.8	2.25
2W-BiVO <sub>4</sub>	2	1.8	15.3	45.0	2.21
5W-BiVO <sub>4</sub>	5	4.4	17.1	47.2	2.14
10W-BiVO <sub>4</sub>	10	7.8	-	49.0	2.13
Zr-Doped nanocatalysts					
0.5Zr-BiVO <sub>4</sub>	0.5	Not detectable	17.8	47.1	2.27
1Zr-BiVO <sub>4</sub>	1	0.4	20.2	45.6	2.25
2Zr-BiVO <sub>4</sub>	2	1.7	19.8	45.7	2.20
5Zr-BiVO <sub>4</sub>	5	3.4	20.5	46.0	2.16
10Zr-BiVO <sub>4</sub>	10	8.3	-	47.2	2.15

\* Data based on average of three batches.

### 2.2. Characterization of Nanocatalysts

X-Ray Diffraction (XRD): The crystal structures of the nanocatalysts were analyzed by XRD in a Bruker Advance D8 diffractometer (Cu K $\alpha$  radiation  $\lambda = 1.5406 \text{ \AA}$ , 40 kV, 40 mA) at  $2\theta = 10\text{--}60^\circ$  (step size of  $0.03^\circ$  at a rate 2 s per step). The average crystallite sizes of BiVO<sub>4</sub>-based particles were calculated by the Scherrer Equation (1):

$$d_{XRD} = \frac{k\lambda}{\beta(\cos\theta)} \quad (1)$$

where  $d_{XRD}$  is the crystallite size (nm),  $k$  is a shape constant (in this case  $k = 0.9$ ),  $\lambda$  is the wavelength of Cu K $\alpha$  radiation ( $1.5406 \text{ \AA}$ ),  $\beta$  is the full-width at half-maximum and  $\theta$  is the peak-diffraction angle.

Brunauer–Emmett–Teller (BET) Analysis: The specific-surface-area (SSA, m<sup>2</sup>/gr) of the synthesized materials was determined by the N<sub>2</sub> adsorption–desorption method at 77 K using a Quantachrome Autosorb-1 instrument (Bounton Beach, FL, USA). In order to acquire the BET isotherms, powders were degassed for 4 h at 120 °C in flowing N<sub>2</sub> over a relative pressure range of  $P/P_0 = 0\text{--}1$ .

X-ray Fluorescence (XRF): Sample excitation was performed with an annular  $^{109}\text{Cd}$  radio-isotopic source (RITVERC GmbH). The source has a radius of 12.5 mm and is housed in a cylindrical container, fixed coaxially above a CANBERRA SL80175 Si(Li) detector (5 mm crystal thickness, 80 mm<sup>2</sup> area), with a 25  $\mu\text{m}$ -thick Be window and an energy resolution of 171 eV for the 5.9 keV Mn K $\alpha$  line. Data acquisition was performed using a PCI card, controlled by the ORTEC MAESTRO-32 software, and spectral analysis was carried out using the WinQxas software package (International Atomic Energy Agency Laboratories Seibersdorf, XRF Group, Seibersdorf (Austria), IAEA 1997–2002).

Raman Spectroscopy: Raman spectroscopy measurements were performed in a HORIBA XploRA PLUS instrument, which employed a 785 nm diode laser as excitation source focused with a microscope. The samples were pressed into pellets and placed on a glass plate. The spectra were recorded for 10 s with 30 accumulations in order to obtain adequate signal-to-noise ratio.

TEM: The morphology of the samples was analyzed by high-resolution transmission electron microscopy (HRTEM) using a Philips CM 20 microscope operated at 200 kV with 0.25 nm resolution. Before the measurements, the samples were ground in a mortar and dry loaded onto a support film (Lacey Carbon, 300 mesh, (Cu)). Recorded images were analyzed by Gatan Digital Micrograph software. Particle-size was calculated using the ImageJ software.

X-ray photoelectron spectroscopy (XPS) data were acquired in a surface analysis ultrahigh vacuum system (SPECS GmbH) equipped with a twin Al-Mg anode X-ray source and a multichannel hemispherical sector electron analyzer (HSA-Phoibos 100). The base pressure was  $2\text{--}5 \times 10^{-9}$  mbar. A monochromatized Mg-K $\alpha$  line at 1253.6 eV and analyzer pass energy of 20 eV were used in all XPS measurements. The binding energies were calculated with reference to the energy of C1s peak of adventitious carbon at 284.5 eV. The peak deconvolution was performed using a Shirley background.

### 2.3. Catalytic Evaluation

The photocatalytic O<sub>2</sub>-evolution experiments were performed using an immersion-well reactor (Photochemical Reactors Ltd., Berkshire UK, Model 3210), provided with two angle sockets and one vertical socket of total reaction volume of 300 mL, being under tap water circulation, at constant temperature  $25 \pm 3$  °C. Light source was an inlet medium-pressure mercury lamp (Model 3010, 125 W, light output  $7 \times 10^{18}$  photons/sec). In each experiment, 50 mg of the catalyst was suspended into 150 mL milli-Q water, which contained 0.1 M NaOH (pH  $\approx$  13.3) and 0.02 M Na<sub>2</sub>S<sub>2</sub>O<sub>8</sub> (final concentration of catalyst 0.2 g/L). Before the reaction begins, the suspension was bubbled with Ar gas (99.997%) at least 1 h, in order to remove atmospheric gas. The experiments with Au were carried out using hydrogen-tetrachloroaurate(III)-trihydrate (HAuCl<sub>4</sub>·3H<sub>2</sub>O, 99.9%, Alfa Aesar, Kandel Germany) as a precursor. Qualitative and quantitative monitoring of produced H<sub>2</sub> was succeeded via a continuous online gas chromatography system combined with a thermo-conductive detector (GC-TCD Shimadzu GC-2014, Carboxen 1000 column, Ar carrier gas).

## 3. Results

### 3.1. Characterization of the FSP-Made BiVO<sub>4</sub>-Based Photocatalysts

XRD: The X-Ray diffraction patterns for all FSP-prepared BiVO<sub>4</sub> nanoparticles are presented in Figure 1. Pristine BiVO<sub>4</sub> is also included for comparison. The coexistence of monoclinic-scheelite (see \* marks) and tetragonal-scheelite phases is apparent in all cases (JCPDS card 75-2480, JCPDS 14-0133) respectively. The structural characterization results of the present nanocatalysts are summarized in Table 1.

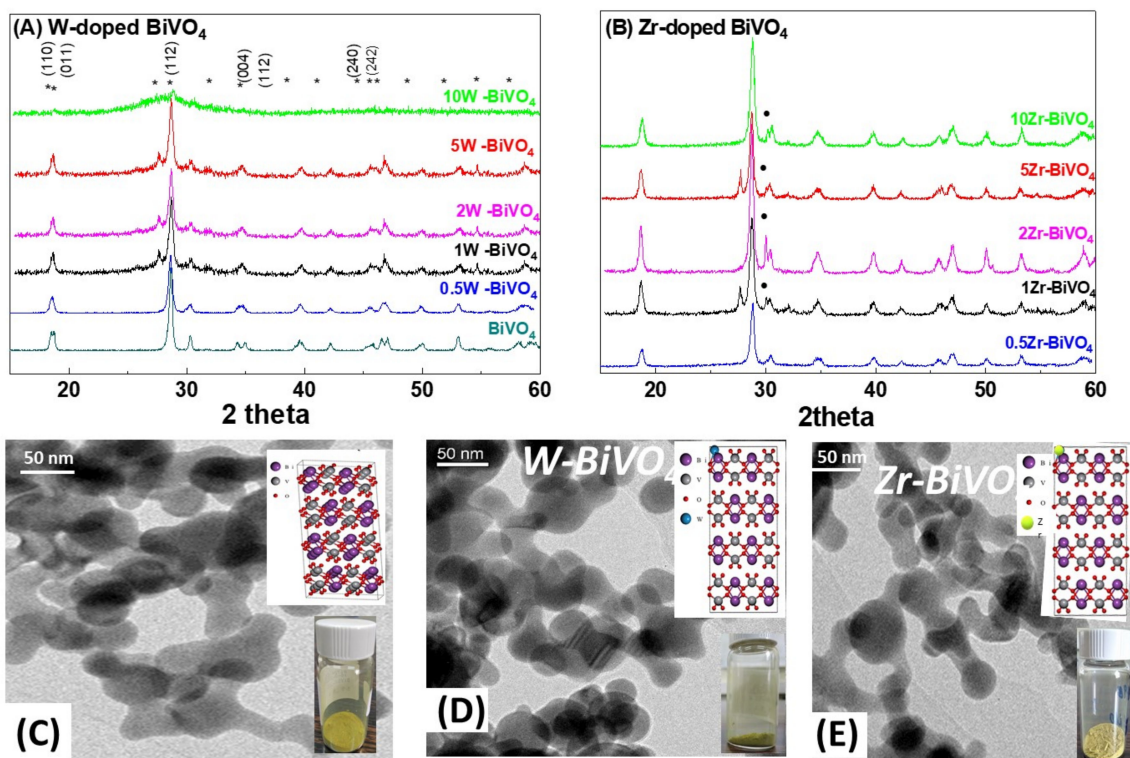


**Figure 1.** XRD patterns (upper row, W-doped (A) and Zr-doped (B)), and TEM images (lower row) for BiVO<sub>4</sub> (C), 5W-BiVO<sub>4</sub> (D) and 5 Zr-BiVO<sub>4</sub> (E). Inserts in C-E: photos of the nanopowders and atomic structure of the materials. In figure also presented the miller index of BiVO<sub>4</sub> structure. In (A), stars (\*) mark the main Miller-planes of BiVO<sub>4</sub>. In (B) the dots (•) mark ZrO<sub>2</sub> phase.

It is known that the monoclinic-scheelite BiVO<sub>4</sub> phase can be obtained from the irreversible phase transformation of tetragonal-zircon structure at temperatures > 400 °C [4,18]. In accordance with [18], in FSP-made pristine BiVO<sub>4</sub>, crystallization of monoclinic-scheelite occurred at temperatures >340 °C. In the XRD data in Figure 1, the peak-splitting of diffraction peaks at  $2\theta = 18.5, 35$  and  $46^\circ$  evidence the presence of the monoclinic-scheelite phase, at all BiVO<sub>4</sub> based nanomaterials. The XRD-derived particle sizes are listed in Table 1. In general, W- or Zr-doping caused rather minor changes in the particle sizes and SSA, see Table 1. In doped-materials, diffraction peaks from secondary phases such as BiWO<sub>4</sub> at  $2\theta = 17.2^\circ$  were detected [9]. Apart from this, W-doping had no effect on the BiVO<sub>4</sub> peak positions, neither BiVO<sub>4</sub> phase-change, i.e., from monoclinic to tetragonal. The present XRD data indicate that in W-doping up to 5% did not change the crystal structure of BiVO<sub>4</sub>. In contrary, a higher W-doping (10%) caused a major deterioration of the crystallinity, i.e., a broad XRD pattern is observed, see Figure 1A. Herein, this material was not further considered for photocatalysis.

In Zr-doped BiVO<sub>4</sub>, certain XRD peaks appeared to be affected, e.g., see the BiVO<sub>4</sub> diffraction at  $2\theta = 18^\circ$  in Figure 1B, while at Zr-doping > 1% diffraction peaks attributed to ZrO<sub>2</sub> particles (back dots in Figure 1B) can be observed. Analysis of the XRD patterns (see Figure S1 in Supporting Information) shows that these corresponded to cubic-ZrO<sub>2</sub> nanoparticles of 3 nm diameter.

The TEM images, Figure 1, show the formation of neck-sintered structures, which is in accordance with the original work for FSP-made BiVO<sub>4</sub> [18]. Such neck-sintered aggregates formations has also been reported recently also for other Bi-based, i.e., BiFeO<sub>3</sub> nanoparticles made by FSP [22].

Raman spectroscopy: Figure 2 illustrates Raman spectra for the FSP-made nanomaterials. In all the spectra, the characteristic vibration peaks from BiVO<sub>4</sub> were detected of all materials. The peaks at 330 and 373 cm<sup>-1</sup> were assigned to the asymmetric and bending

vibrations of  $\text{VO}_4^{3-}$  unit respectively [18]. The peak at  $830\text{cm}^{-1}$ , marked as V-O(s) in Figure 2, can be attributed to stretching vibrations of the V-O bonds in the  $\text{VO}_4^{3-}$  unit [12]. The position of Raman peak at  $830\text{cm}^{-1}$  gives information on the V-O on length [12] thus is a good indicator for distortions of the overall lattice. In the doped  $\text{BiVO}_4$  materials, Figure 2, we observe that the V-O(s) band position at  $830\text{cm}^{-1}$  is gradually downshifted, see inset in Figure 2A,B for increased W- and Zr-doping percentage respectively. These shifts indicate gradual deformation of  $\text{VO}_4^{3-}$  unit, due to insertion of the W- or Zr-atoms into the  $\text{BiVO}_4$  crystal. Notice that these lattice deformations could only be probed by Raman, while they were not resolved in the XRD.

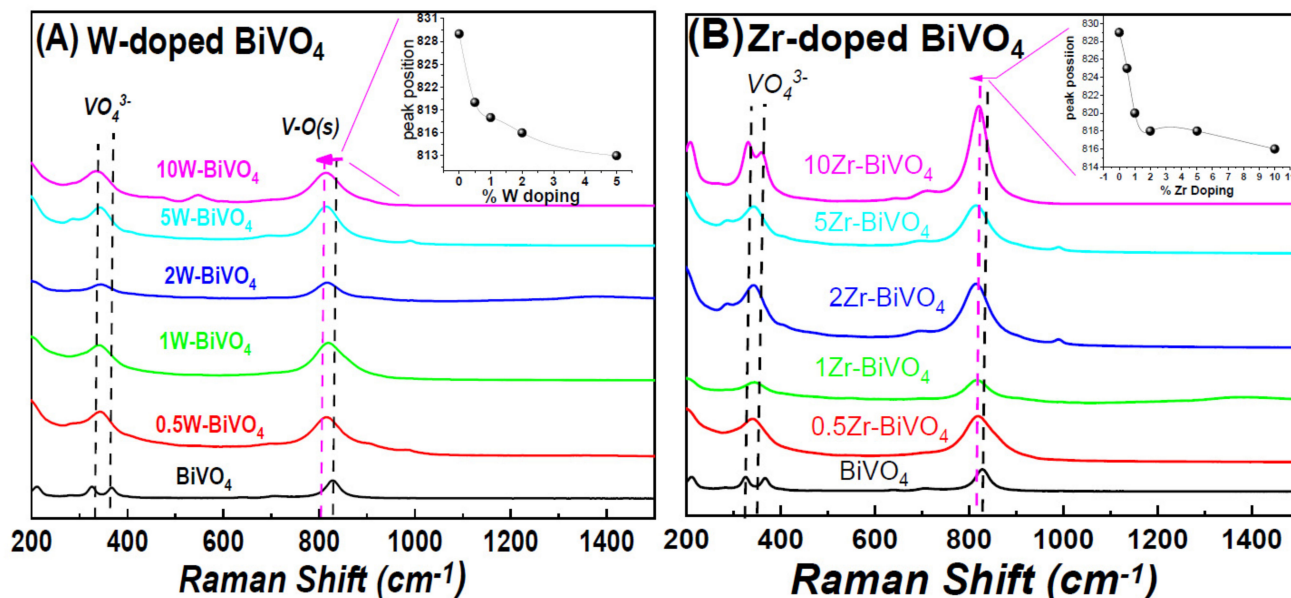


**Figure 2.** Raman spectra for the FSP-made  $\text{BiVO}_4$ -based photocatalysts: (A) W-doped nanomaterials and (B) Zr-doped nanomaterials. Inset: shift of Raman V-O(s) peak at  $830\text{cm}^{-1}$ .

X-ray Photoelectron Spectroscopy (XPS): Representative broad-scan XPS data for FSP-made  $\text{BiVO}_4$ -based materials are presented in Figure 3. In all cases, the XPS data confirm the presence of Bi, V and O, while no peaks assignable to W or Zr can be discerned in the 5%W or 5%Zr materials. However, affirmative evidence for the presence of the dopant species is confirmed by our XRF spectroscopy data (see Table 1). The  $\text{Bi}_{4f5/2}$  and  $\text{Bi}_{4f7/2}$  binding energies at 164.2 and 158.7 eV respectively, were well resolved for all the photocatalysts. The  $\text{V}_{2p3/2}$  peak is also resolved in all cases. The  $\text{O}_{1s}$  binding energies can be fitted with two peaks, ascribed to the lattice oxygen of  $\text{BiVO}_4$  crystal, and oxygen vacancies formed on the surface of the  $\text{BiVO}_4$  [23,24].

Doping with W or Zr, resulted in an enhancement of the concentration of oxygen vacancies ( $\text{V}_o$ ), see Figure 3. Thus, the XPS data in Figure 3, show that the as-prepared FSP-made  $\text{BiVO}_4$  contains O-vacancies, whose concentration can be promoted by W- or Zr-doping. This phenomenon, i.e., the correlation of W with O-vacancies sites, has been recently discussed in theoretical DFT studies [19,20,24]. More specifically, theoretical calculations indicate that surface O-vacancies enhance the electron density near the bottom of the conduction band of  $\text{BiVO}_4$  [19]. Additionally, there is theoretical evidence [20,24] that O-vacancies may play a role in the interfacial charge transfer. Importantly, the DFT data entail that the role of W-doping is interlinked with the O-vacancies in the enhancement of the photocatalytic electron-hole separation [24]. As we show hereafter, our data on photocatalytic  $\text{O}_2$ -evolution, provide corroborating experimental evidence for the positive effect of W- and Zr-doping in conjunction with the  $\text{V}_o$  in  $\text{BiVO}_4$ .

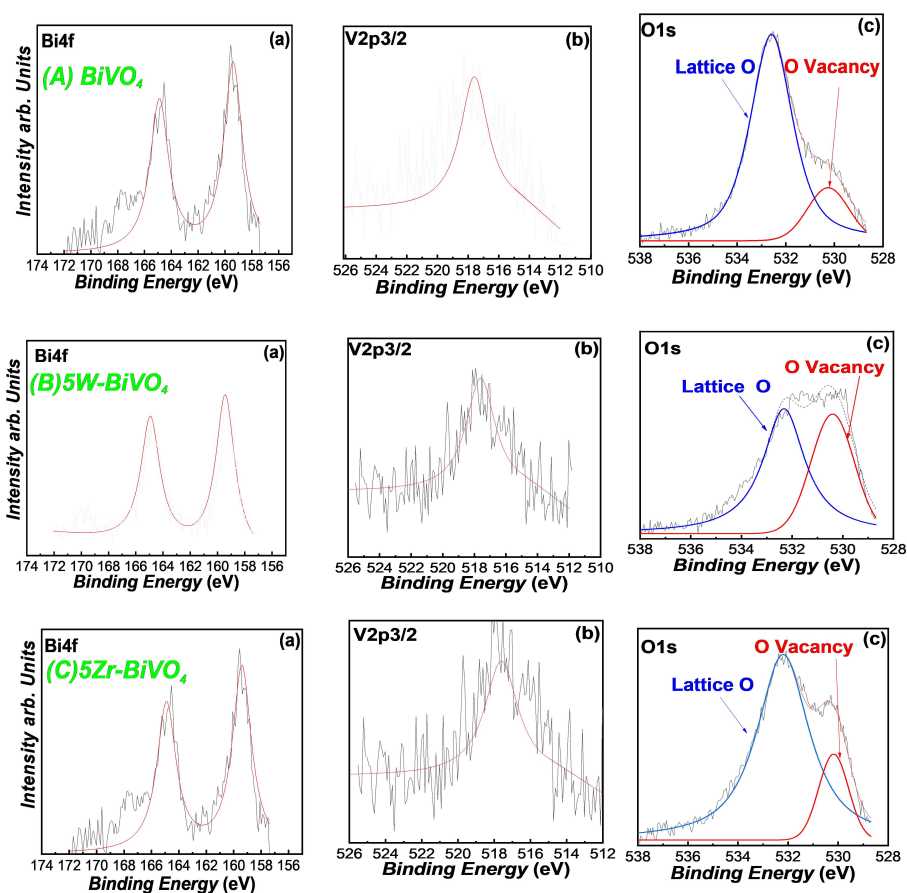


Figure 3. XPS spectra of (A) pristine FSP-made  $\text{BiVO}_4$ , (B) 5W- $\text{BiVO}_4$  and (C) 5Zr- $\text{BiVO}_4$  ((a)  $\text{Bi}_{4f}$ , (b)  $\text{V}_{2p}$  and (c)  $\text{O}_{1s}$ ).

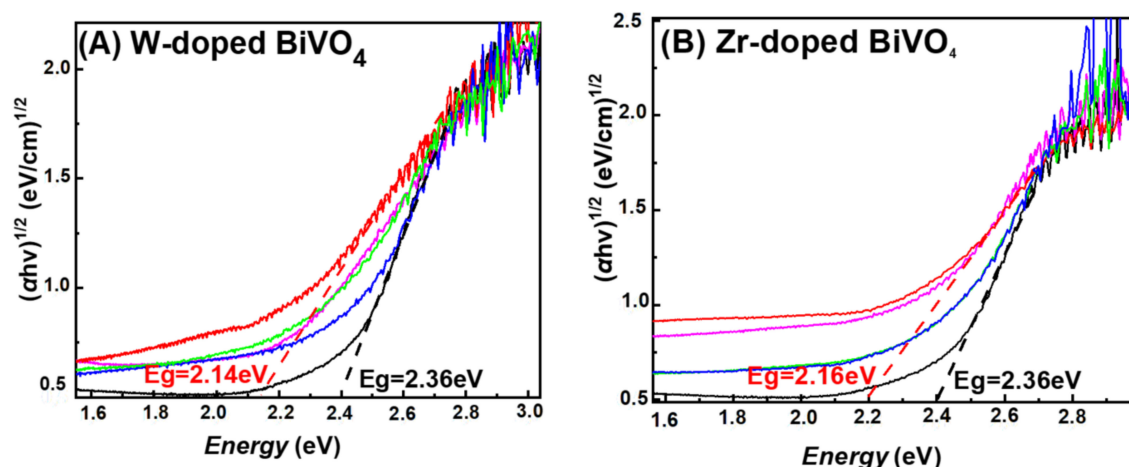
Diffuse Reflectance UV–Vis (DR–UV–Vis): Figure 4 presents DR–UV–Vis spectra and optical band gap energy determination using the Kubelka–Munk [25] formula (2) where  $\alpha$  is the absorption coefficient, and the  $n$ -value is related to the type of photoexcited transition, i.e., direct or indirect [25].

$$\alpha h\nu = A(h\nu - E)^{n/2} \quad (2)$$

In our analysis, a value of  $n = 2$  was set, i.e., since  $\text{BiVO}_4$  is a direct band gap semiconductor [25].

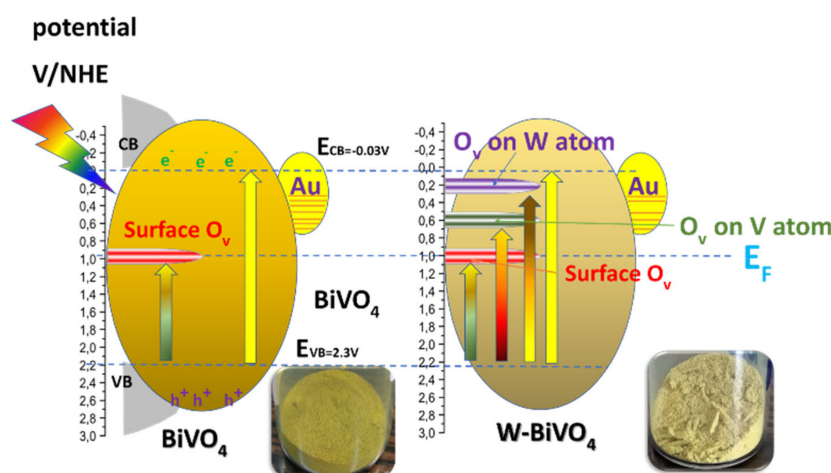
All our FSP-made materials showed adsorption edges with a tail extending towards low-energies, which was enhanced at increasing W- or Zr-doping, see Figures 4A and 4B respectively. Optical band gap energies estimated from the DR–UV–Vis data, are marked by the tangent lines in Figure 4, while the full list of  $E_g$  values are presented in Table 1. A band-gap value of  $E_g = 2.36$  eV is typical for pristine  $\text{BiVO}_4$  [24]. Notice that pristine  $\text{BiVO}_4$  showed also a low-energy tail, i.e., resolved as a weak hump at 1.6 eV in Figure 4A. This can be attributed to low-energy photons absorbed via intraband states created by the oxygen-vacancies [24] at the Fermi level of  $\text{BiVO}_4$ .

Figure 5 presents a schematic depiction of the energy profile of our  $\text{BiVO}_4$ -based particles. Doping causes a progressive decrease of the  $E_g$  values, see Figure 4 and Table 1, i.e., the  $E_g$  was progressively decreased to 2.14 eV for 5W- $\text{BiVO}_4$  and  $E_g = 2.16$  eV for 5Zr- $\text{BiVO}_4$ . As analyzed previously in detail, for W-doped  $\text{BiVO}_4$  [19,20] these trends can be attributed to creation of intraband states, see Figure 5 (right). DFT calculations [5,19,20,24] indicate that the energy of the intraband states is sensitive to the exact location of the W-atom, i.e., whether an oxygen-vacancy occurs next to a W- or next to a V-atom [24], see Figure 5.



**Figure 4.** Kubelka–Munk transformed diffuse reflectance UV–Vis spectra of FSP-made  $\text{BiVO}_4$ -based nanocatalysts. (A) W-doped  $\text{BiVO}_4$  and (B) Zr-doped  $\text{BiVO}_4$ .

In our materials, in all cases, the  $E_g$  decrease was accompanied by enhanced light-absorbance at low-energies, verifying that such intraband states are indeed formed upon insertion of the W- or Zr-heteroatoms in to the  $\text{BiVO}_4$  lattice [24]. Notice that such low-energy light-absorbance is manifested in a more-opaque, less-sharp yellowish color of the W- $\text{BiVO}_4$  and Zr- $\text{BiVO}_4$  materials, see photos of the FSP-powders in Figure 5. Accordingly, we consider that in our FSP-made  $\text{BiVO}_4$ , all the possible intraband states depicted in Figure 5 (right) might be formed, thus a quasi-continuum of low-energy photons are absorbed by the doped  $\text{BiVO}_4$  materials.



**Figure 5.** Schematic depiction of the energy levels of FSP-made photocatalysts. Surface O-vacancies create Fermi-level states in  $\text{BiVO}_4$  (left). In addition, W-doping (right) generates additional intraband states whose position depends on the relative location of W, V atoms and O-vacancies [24].

Overall, the present XPS, Raman and DRS-UV–Vis data provide converging evidence that: (i) our FSP-made  $\text{BiVO}_4$  contains oxygen vacancies. (ii) W-doping and Zr-doping increase the population of the oxygen vacancies. (iii) W-doping and Zr-doping generate intraband energy states, which enhance the photon-absorbance profile at increased wavelengths, i.e., lower energies down to 50% of the original  $E_g$ . These observations are of immediate relevance to the photocatalytic  $\text{O}_2$ -evolution, as we show in the following.

### 3.2. Catalytic Results

#### 3.2.1. Photocatalytic O<sub>2</sub>-Evolution from H<sub>2</sub>O

The photocatalytic water oxidation activity of our BiVO<sub>4</sub>-based catalysts was investigated, using Au as cocatalyst. Figure 6A,B presents data on the O<sub>2</sub> evolution kinetics, for the W- and Zr-doped BiVO<sub>4</sub>-based catalysts.

The data in Figure 6 show that all photocatalysts produced O<sub>2</sub> from H<sub>2</sub>O splitting. More precisely, after 180 min of irradiation, the O<sub>2</sub> generated by the best-performing catalyst, 5W-BiVO<sub>4</sub>, was 2217 μmol per g of material, Figure 6A. The homologous material 5Zr-BiVO<sub>4</sub> produced 3018 μmol/g within 180 min of reaction, Figure 6B. For comparison, Figure 6C,D presents the O<sub>2</sub> evolution activities in (μmoles per gram of catalyst) at t = 180 min, based on the data of Figure 6A,B. The data are summarized in Table 2.

According to Figure 6E and Table 2, W-doping even at 0.5% resulted in a drastic improvement of the O<sub>2</sub> evolution activity vs. pristine BiVO<sub>4</sub>. Among them, 5 W-BiVO<sub>4</sub> exhibited a 270% higher activity than pristine BiVO<sub>4</sub> under the same catalytic conditions. When we compared the W-doped vs. Zr-doped materials in Figure 6E, we noticed that significantly higher Zr-doping is required to achieve comparable O<sub>2</sub> production rate, as for W-doping. Take as example the 0.5%-doped materials: O<sub>2</sub> production rate was 633 μmol/(g × h) for 0.5% W doped vs. 235 μmol/(g × h) for the 0.5% Zr-doped BiVO<sub>4</sub>. Notice that the two materials had analogous specific-surface-area, i.e., 45 m<sup>2</sup>/gr vs. 47 m<sup>2</sup>/g, see Table 1. Thus, if we would normalize per SSA, the W-doped material far more active than the Zr doped BiVO<sub>4</sub>. In all cases, high dopant-loading, i.e., 10%W or 10%Zr, resulted to lower O<sub>2</sub>-evolution efficiency.

**Table 2.** O<sub>2</sub>-evolution by the present FSP-made BiVO<sub>4</sub>-based photocatalysts.

Material	O <sub>2</sub> -Evolution (μmol/g) after 3 h Reaction	O <sub>2</sub> -Evolution Rate (μmol/g × h)
BiVO <sub>4</sub>	1249 (±20)	420 (±5)
	W-Doped nanocatalysts	
0.5W-BiVO <sub>4</sub>	1842 (±20)	633 (±5)
1W-BiVO <sub>4</sub>	2002 (±20)	667 (±5)
2W-BiVO <sub>4</sub>	2827 (±20)	945 (±5)
5W-BiVO <sub>4</sub>	3326 (±20)	1020 (±5)
10W-BiVO <sub>4</sub>	2100 (±20)	778 (±5)
	Zr-Doped nanocatalysts	
0.5Zr-BiVO <sub>4</sub>	600 (±20)	235 (±5)
1Zr-BiVO <sub>4</sub>	1039 (±20)	337 (±5)
2Zr-BiVO <sub>4</sub>	1512 (±20)	521 (±5)
5Zr-BiVO <sub>4</sub>	3018 (±20)	974 (±5)
10 Zr-BiVO <sub>4</sub>	907 (±20)	324 (±5)
	Calcined nanocatalysts	
5W-BiVO <sub>4</sub> @200	2804 (±20)	1001 (±5)
5W-BiVO <sub>4</sub> @360	1973 (±20)	720 (±5)
5Zr-BiVO <sub>4</sub> @200	1988 (±20)	710 (±5)
5Zr-BiVO <sub>4</sub> @360	1299 (±20)	448 (±5)

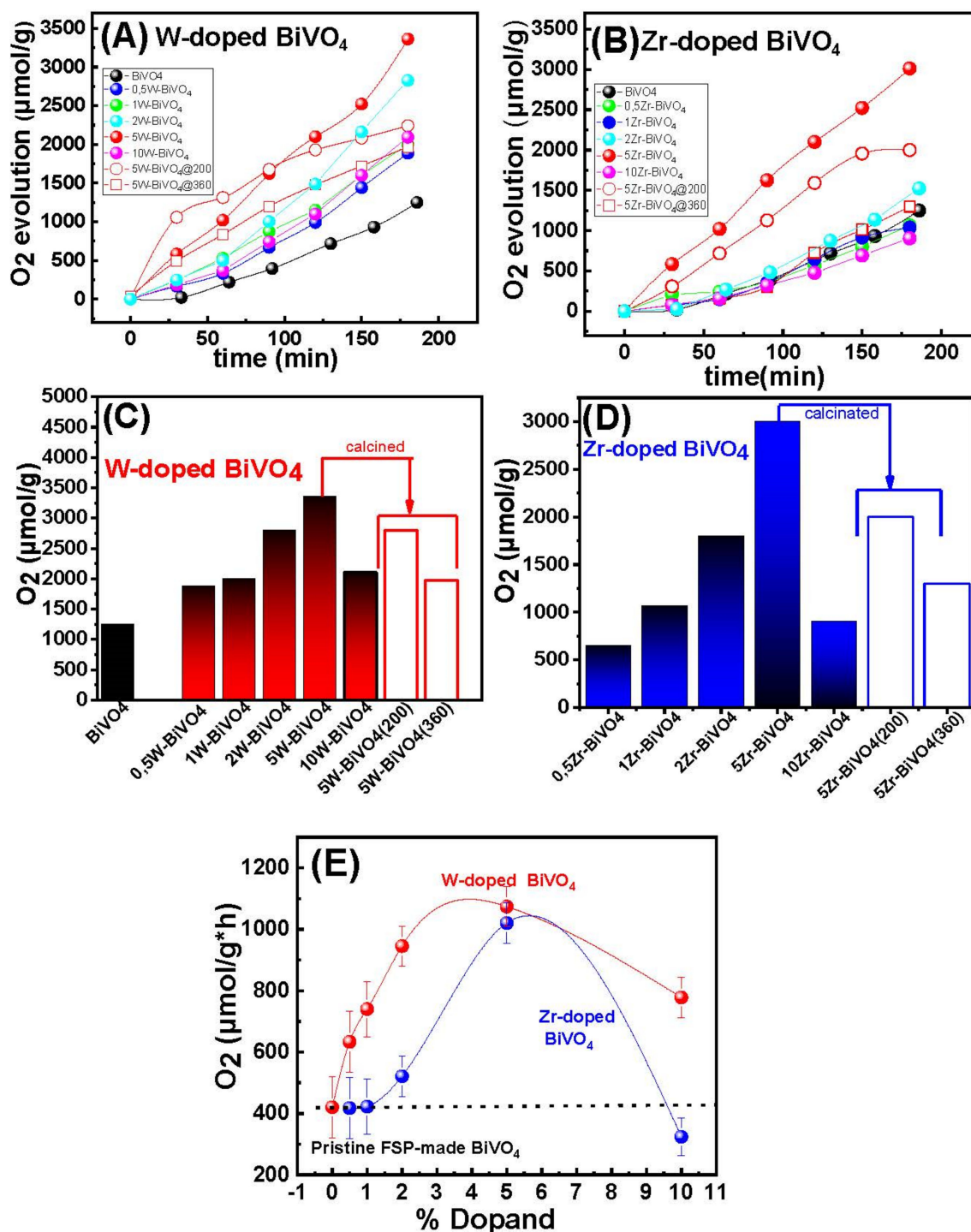


**Figure 6.** (A) Kinetics of O<sub>2</sub>-evolution by the W-BiVO<sub>4</sub> and (B) O<sub>2</sub> evolution by Zr-BiVO<sub>4</sub>. Solid symbols are for as prepared materials. Open symbols for calcined at 200 °C (open circles), or 360 °C (open squares). (C) Comparison of O<sub>2</sub>-evolution efficiencies of the present FSP-photocatalysts after 180 min of photocatalytic reaction (W-BiVO<sub>4</sub>), (D) (Zr-BiVO<sub>4</sub>) and (E) O<sub>2</sub> evolution rate vs. the dopant loading. The lines in (E) are for guiding the eye.

### 3.2.2. Comparison with Literature

In Table 3 we listed the O<sub>2</sub> evolution rates (μmol/g × h) reported so far for pertinent BiVO<sub>4</sub> based photocatalysts, synthesized with various methods or doped with different ions.

**Table 3.** Comparison of the O<sub>2</sub> evolution rate from BiVO<sub>4</sub>-based photocatalysts.

Photocatalyst	Light Source	Synthesis Method	XRD Size (nm)	Electron Acceptor	Activity (μmol/g <sup>3</sup> h)	Ref.
BiVO <sub>4</sub>	400 W medium-pressure halide lamp (Phillips HPA400, λ <sub>max</sub> = 360 nm)	Hydrothermal method	28.3	AgNO <sub>3</sub>	2622	[26]
BiVO <sub>4</sub>	300 W Xe lamp with a 420 nm cut off filter	Flame Synthesis of BiVO <sub>4</sub> and Acid Modification	72.0	AgNO <sub>3</sub>	333	[27]
BiVO <sub>4</sub>	300 W Xe lamp with a 420 nm cut off filter	Solid-liquid state reaction in HNO <sub>3</sub>	91.0	AgNO <sub>3</sub>	800	[28]
Ce-BiVO <sub>4</sub>	300 W Xe lamp	Hydrothermal method	Not referred	AgNO <sub>3</sub>	775	[14]
A-FeOOH/BiVO <sub>4</sub> (8 wt %)	300 W Xe lamp with a 420 nm cut off filter	Precipitation method	Not referred	NaIO <sub>4</sub>	1206	[29]
Zr-BiVO <sub>4</sub>	Perkin Elmer CERMAX LX-300BUV Xe lamp	Precipitation method	Not referred	AgNO <sub>3</sub>	700	[13]
W(0.9%w/w)-BiVO <sub>4</sub>	Simulated plasma (Lumix model LIFI STA-40)	Hydrothermal method	92.0	AgNO <sub>3</sub>	942	[30]
BiVO <sub>4</sub>	125W Hg λ <sub>max</sub> = 440 nm	FSP	22.1	AuHCl <sub>4</sub>	420	This work
5W-BiVO <sub>4</sub>	125W Hg λ <sub>max</sub> = 440 nm	FSP	17.1	AuHCl <sub>4</sub>	1074	This work
5Zr-BiVO <sub>4</sub>	125W Hg λ <sub>max</sub> = 440 nm	FSP	20.5	AuHCl <sub>4</sub>	1020	This work

The data in Table 3 show that the present 5W-BiVO<sub>4</sub> and 5Zr-BiVO<sub>4</sub> ranked among the best-performing O<sub>2</sub>-evolving photocatalysts. Taking into account the differences in the photon-flux, i.e., low-light 125 W of our irradiation system vs. 400 W in reference [26], further confirms that the present FSP-made materials stand at high performance rank. Our data exemplified that a concomitant control of O-vacancies and W-doping is a potent route for engineering of efficient low-cost O<sub>2</sub>-evolving photocatalysts.

### 3.2.3. Reusability of the Nanocatalysts

Among the main aims of the heterogeneous catalysis is the reusability of the catalyst. In the present work, the reusability of our best-performing photocatalyst, 5W-BiVO<sub>4</sub> was evaluated. After each catalytic use, the solid catalyst was recovered by centrifugation (6000 rpm, 15 min). The liquid supernatant was discarded, and the solid was used for a new reaction under the same catalytic conditions—with no further addition of catalyst.

According to Figure 7, after four sequential catalytic cycles the 5W-BiVO<sub>4</sub> catalyst retained 75% of its catalytic activity. The moderate loss of the catalytic activity is progressive and can be attributed to the loss of material mass at each centrifugation–recovery–reuse step, and aggregation phenomena of the particles as reported previously for other BiVO<sub>4</sub> particles [26,28].

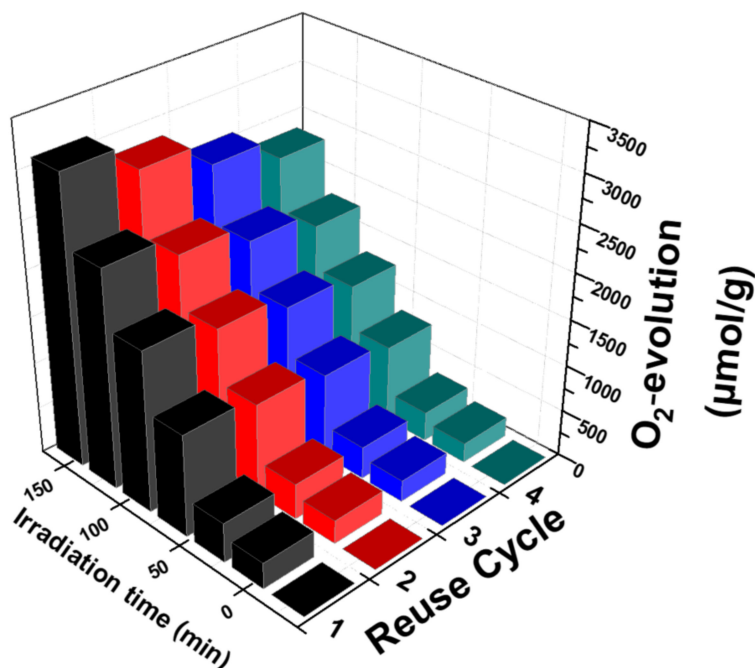


Figure 7. Photocatalytic O<sub>2</sub> evolution by sequential reuse of the same 5W-BiVO<sub>4</sub>-batch.

#### 4. On the Mechanism of Photocatalytic Oxygen Evolution

Previous theoretical calculations suggest that surface oxygen-vacancies enhance the electron density near the bottom of the conduction band of BiVO<sub>4</sub> [24]. Moreover, Vo and W-doping may play an important role in the interfacial charge transfer, and in this way W-doping is interlinked with the Vo [19,24] and the enhancement of the photocatalytic electron-hole separation [19,20,24]. To verify the role of the oxygen-vacancies, herein we oxidized, i.e., by mild calcination under O<sub>2</sub>, the best performing 5 W-BiVO<sub>4</sub> and 5 Zr-BiVO<sub>4</sub> particles.

The data, see Figure 6C (open bars), show a sharp drop in O<sub>2</sub>-production efficiency as a function of the calcination temperature. The XRD data, see Figure S2 in Supporting Information, show an increase of particle size, i.e., it becomes 37 nm upon calcination at 360 °C for 3 h. At the same time, the Raman spectra, Figure S3 in Supporting Information, show a restoration of the peak position of the V-O(s) mode at 830 cm<sup>-1</sup> indicating the elimination of the O-vacancies from the lattice of W-BiVO<sub>4</sub>. Moreover, there is a strong correlation of calcination with the decline of the O-vacancies population as detected by XPS, see Figure 8. An analogous phenomenon has been reported by other researchers also [21,24,25,31]. Here, our data allow a better comprehension of the necessity of W-doping and O-vacancies occurrence for enhancing O<sub>2</sub>-evolution. W-doping alone, i.e., without O-vacancies does not suffice for enhanced O<sub>2</sub>-evolution. Notice that in Figure 6C, after calcination at 360 °C the efficiency of the best-performing 5W-BiVO<sub>4</sub> dropped below the non-doped BiVO<sub>4</sub>.

In agreement with previous reports, [31], the present data show that the primary factor for enhanced O<sub>2</sub>-evolution is the optimal O-vacancy engineering. Herein the 5W-BiVO<sub>4</sub> and 5 Zr-BiVO<sub>4</sub> materials, when oxidized by calcination at mild temperatures 200 °C and 360 °C for 3 h under air their O<sub>2</sub>-production declined from 3326 μmol/g to 2804 μmol/g and 1973 μmol/g. Analogous results observed for the 5 Zr-BiVO<sub>4</sub> (see Table 2, and Figure 6).

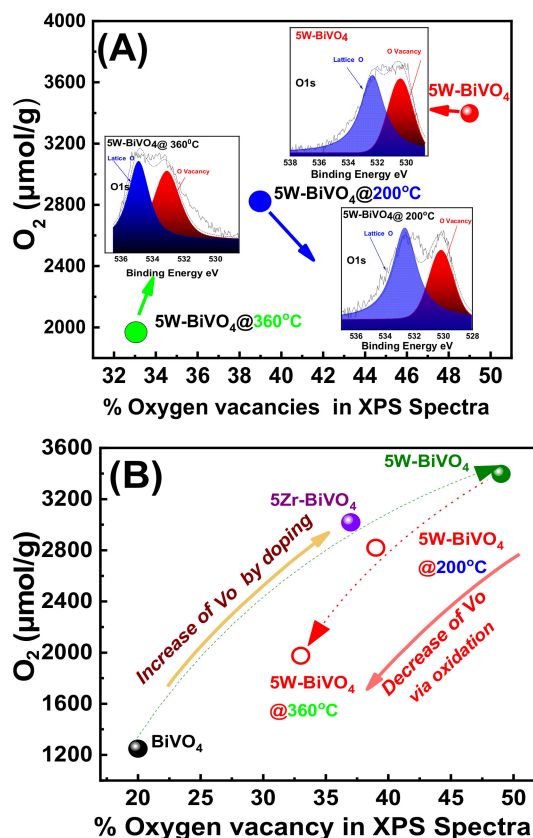


**Figure 8.** Photocatalytic O<sub>2</sub>-evolution evolution vs. the O-vacancies in the doped-BiVO<sub>4</sub> catalysts. (A) Increase of O-vacancies is promoted by W- or Zr-doping in FSP-made BiVO<sub>4</sub>. Inset: O 1s XPS spectra of the W-doped BiVO<sub>4</sub>. (B) Calcination under O<sub>2</sub>-rich atmosphere (oxidation) results in decrease of O-vacancies.

## 5. Conclusions

The present research bears two key-results (i) FSP-technology allows engineering of oxygen vacancies content in BiVO<sub>4</sub> via W-doping or Zr-doping, and (ii) oxygen-vacancies are the primary factor to determine the photocatalytic O<sub>2</sub>-production via water oxidation. FSP allows engineering of BiVO<sub>4</sub> nanoparticles, with controlled heteroatom-dopant content, and oxygen vacancy content. As a proof of concept, W- and Zr-doped BiVO<sub>4</sub> photocatalysts prepared with different dopant loading were engineered. The correlation between the catalytic efficiency and the oxygen-vacancies content provides strong evidence that the presence of oxygen vacancies in W-BiVO<sub>4</sub>, Zr-BiVO<sub>4</sub> improves drastically the O<sub>2</sub> production efficiency. Our present data on doped BiVO<sub>4</sub> corroborate the mechanistic suggestions, indicating that the beneficial role of oxygen vacancy is a general phenomenon, which should be operating in various photocatalysts.

**Supplementary Materials:** The following are available online at <https://www.mdpi.com/2079-4991/11/2/501/s1>, Figure S1: theoretical simulation of XRD patterns, Figure S2: XRD data for W doped BiVO<sub>4</sub>. Figure S3: Raman spectra of calcined W doped BiVO<sub>4</sub>.

**Author Contributions:** P.S. and M.S.: Data curation, Writing- Original draft preparation. Y.D.: Supervision, Writing- Reviewing and Editing. All authors have read and agreed to the published version of the manuscript.

**Funding:** The research work was supported by the Hellenic Foundation for Research and Innovation (H.F.R.I) under the “First Call for H.F.R.I Research Projects to support Faculty members and Researchers and the procurement of high-cost research equipment grant” (Project Number: HFRI-FM17-1888).

**Data Availability Statement:** Data is available upon the reasonable request from the corresponding author.

**Conflicts of Interest:** The authors declare no conflict of interest.

## References

1. Fujishima, A.; Honda, K. Electrochemical Photolysis of Water at a Semiconductor Electrode. *Nature* **1972**, *238*, 37–38. [[CrossRef](#)]
2. Kudo, A.; Ueda, K.; Kato, H.; Mikami, I. Photocatalytic O<sub>2</sub> evolution under visible light irradiation on BiVO<sub>4</sub> in aqueous AgNO<sub>3</sub> solution. *Catal. Lett.* **1998**, *53*, 229–230. [[CrossRef](#)]
3. Moniz, S.J.A.; Shevlin, S.A.; Martin, D.J.; Guo, Z.X.; Tang, J. Visible-light driven heterojunction photocatalysts for water splitting—a critical review. *Energy Environ. Sci.* **2015**, *8*, 731–759. [[CrossRef](#)]
4. Kato, H.; Hori, M.; Kanta, R.; Shimodaira, Y.; Kudo, A. Construction of Z-scheme type heterogeneous photocatalysis systems for water splitting into H<sub>2</sub> and O<sub>2</sub> under visible light irradiation. *Chem. Lett.* **2004**, *33*, 1348–1349. [[CrossRef](#)]
5. Abdi, F.F.; Savenije, T.J.; May, M.M.; Dam, B.; Van De Krol, R. The Origin of Slow Carrier Transport in BiVO<sub>4</sub> Thin Film Photoanodes. *J. Phys. Chem. Lett.* **2013**, *4*, 2752–2757. [[CrossRef](#)]
6. Zhang, B.; Zhang, H.; Wang, Z.; Zhang, X.; Qin, X.; Dai, Y.; Liu, Y.; Wang, P.; Li, Y.; Huang, B. Doping strategy to promote the charge separation in BiVO<sub>4</sub> photoanodes. *Appl. Catal. B Environ.* **2017**, *211*, 258–265. [[CrossRef](#)]
7. Ding, K.; Chen, B.; Fang, Z.; Zhang, Y.; Chen, Z. Why the photocatalytic activity of Mo-doped BiVO<sub>4</sub> is enhanced: A comprehensive density functional study. *Phys. Chem. Chem. Phys.* **2014**, *16*, 13465–13476. [[CrossRef](#)] [[PubMed](#)]
8. Shan, L.; Liu, H.; Wang, G. Preparation of tungsten-doped BiVO<sub>4</sub> and enhanced photocatalytic activity. *J. Nanopart. Res.* **2015**. [[CrossRef](#)]
9. Yang, Y.; Zhao, Y.; Fan, W.; Shen, H.; Shi, W. A simple flame strategy for constructing W-doped BiVO<sub>4</sub> photoanodes with enhanced photoelectrochemical water splitting. *Int. J. Energy Res.* **2020**, *44*, 10821–10831. [[CrossRef](#)]
10. Ngoipala, A.; Ngamwongwan, L.; Fongkaew, I.; Jungthawan, S.; Hirunsit, P.; Limpijumngong, S.; Suthirakun, S. On the Enhanced Reducibility and Charge Transport Properties of Phosphorus-Doped BiVO<sub>4</sub> as Photocatalysts: A Computational Study. *J. Phys. Chem. C* **2020**, *124*, 4352–4362. [[CrossRef](#)]
11. Babu, P.; Mohanty, S.; Naik, B.; Parida, K. Serendipitous Assembly of Mixed Phase BiVO<sub>4</sub> on B-Doped g-C<sub>3</sub>N<sub>4</sub>: An Appropriate p-n Heterojunction for Photocatalytic O<sub>2</sub> evolution and Cr(VI) reduction. *Inorg. Chem.* **2019**, *58*, 12480–12491. [[CrossRef](#)]
12. Jiang, Z.; Liu, Y.; Jing, T.; Huang, B.; Zhang, X.; Qin, X.; Dai, Y.; Whangbo, M.H. Enhancing the Photocatalytic Activity of BiVO<sub>4</sub> for Oxygen Evolution by Ce Doping: Ce<sup>3+</sup> Ions as Hole Traps. *J. Phys. Chem. C* **2016**, *120*, 2058–2063. [[CrossRef](#)]
13. Ikeda, S.; Kawaguchi, T.; Higuchi, Y.; Kawasaki, N.; Harada, T. Effects of Zirconium Doping into a Monoclinic Scheelite BiVO<sub>4</sub> Crystal on Its Structural, Photocatalytic, and Photoelectrochemical Properties. *Front. Chem.* **2018**, *6*, 2–7. [[CrossRef](#)]
14. Yin, W.; Wei, S.; Al-jassim, M.M.; Turner, J.; Yan, Y. Doping properties of monoclinic BiVO<sub>4</sub> studied by first-principles density-functional theory. *Phys. Rev. B* **2011**, *155102*, 1–11.
15. Parmar, K.P.S.; Kang, H.J.; Bist, A.; Dua, P.; Jang, J.S.; Lee, J.S. Photocatalytic and photoelectrochemical water oxidation over metal-doped monoclinic BiVO<sub>4</sub> photoanodes. *ChemSusChem* **2012**, *5*, 1926–1934. [[CrossRef](#)]
16. Camenzind, A.; Caseri, W.R.; Pratsinis, S.E. Flame-made nanoparticles for nanocomposites. *Nano Today* **2010**, *5*, 48–65. [[CrossRef](#)]
17. Teoh, W.Y.; Amal, R.; Mädler, L. Flame spray pyrolysis: An enabling technology for nanoparticles design and fabrication. *Nanoscale* **2010**, *2*, 1324–1327. [[CrossRef](#)]
18. Kho, Y.K.; Teoh, W.Y.; Iwase, A.; Mädler, L.; Kudo, A.; Amal, R. Flame preparation of visible-light-responsive BiVO<sub>4</sub> oxygen evolution photocatalysts with subsequent activation via aqueous route. *ACS Appl. Mater. Interfaces* **2011**, *3*, 1997–2004. [[CrossRef](#)] [[PubMed](#)]
19. Wang, W.; Strohbeen, P.J.; Lee, D.; Zhou, C.; Kawasaki, J.K.; Choi, K.-S.; Liu, M.; Galli, G. The Role of Surface Oxygen Vacancies in BiVO<sub>4</sub>. *Chem. Mater.* **2020**, *32*, 2899–2909. [[CrossRef](#)]
20. Zhao, X.; Hu, J.; Yao, X.; Chen, S.; Chen, Z. Clarifying the Roles of Oxygen Vacancy in W-Doped BiVO<sub>4</sub> for Solar Water Splitting. *ACS Appl. Energy Mater.* **2018**, *1*, 3410–3419. [[CrossRef](#)]
21. Moularas, C.; Georgiou, Y.; Adamska, K.; Deligiannakis, Y. Thermoplasmonic Heat Generation Efficiency by Nonmonodisperse Core–Shell Ag@SiO<sub>2</sub> Nanoparticle Ensemble. *J. Phys. Chem. C* **2019**, *123*, 22499–22510. [[CrossRef](#)]
22. Psathas, P.; Georgiou, Y.; Moularas, C.; Armatas, G.S.; Deligiannakis, Y. Controlled-Phase Synthesis of Bi<sub>2</sub>Fe<sub>4</sub>O<sub>9</sub> & BiFeO<sub>3</sub> by Flame Spray Pyrolysis and their evaluation as non-noble metal catalysts for efficient reduction of 4-nitrophenol. *Powder Technol.* **2020**, *368*, 268–277.
23. Wu, J.M.; Chen, Y.; Pan, L.; Wang, P.; Cui, Y.; Kong, D.C.; Wang, L.; Zhang, X.; Zou, J.J. Multi-layer monoclinic BiVO<sub>4</sub> with oxygen vacancies and V<sup>4+</sup> species for highly efficient visible-light photoelectrochemical applications. *Appl. Catal. B Environ.* **2018**, *221*, 187–195. [[CrossRef](#)]
24. Liu, G.; Li, F.; Zhu, Y.; Li, J.; Sun, L. Cobalt doped BiVO<sub>4</sub> with rich oxygen vacancies for efficient photoelectrochemical water oxidation. *RSC Adv.* **2020**, *10*, 28523–28526. [[CrossRef](#)]
25. Walsh, A.; Yan, Y.; Huda, M.N.; Al-Jassim, M.M.; Wei, S.H. Band edge electronic structure of BiVO<sub>4</sub>: Elucidating the role of the Bi s and V d orbitals. *Chem. Mater.* **2009**, *21*, 547–551. [[CrossRef](#)]
26. Chen, S.H.; Jiang, Y.S.; Lin, H.Y. Easy Synthesis of BiVO<sub>4</sub> for Photocatalytic Overall Water Splitting. *ACS Omega* **2020**, *5*, 8927–8933. [[CrossRef](#)]

27. Yoshino, S.; Iwase, A.; Ng, Y.H.; Amal, R.; Kudo, A. Z-Schematic Solar Water Splitting Using Fine Particles of H<sub>2</sub>-Evolving (CuGa)<sub>0.5</sub>ZnS<sub>2</sub> Photocatalyst Prepared by a Flux Method with Chloride Salts. *ACS Appl. Energy Mater.* **2020**, *3*, 5684–5692. [[CrossRef](#)]
28. Tan, H.L.; Amal, R.; Ng, Y.H. Exploring the Different Roles of Particle Size in Photoelectrochemical and Photocatalytic Water Oxidation on BiVO<sub>4</sub>. *ACS Appl. Mater. Interfaces* **2016**, *8*, 28607–28614. [[CrossRef](#)]
29. Zhang, Y.; Shi, L.; Geng, Z.; Ren, T.; Yang, Z. The improvement of photocatalysis O<sub>2</sub> production over BiVO<sub>4</sub> with amorphous FeOOH shell modification. *Sci. Rep.* **2019**, *9*, 2–11. [[CrossRef](#)] [[PubMed](#)]
30. Thalluri, S.M.; Hernández, S.; Bensaid, S.; Saracco, G.; Russo, N. Green-synthesized W- and Mo-doped BiVO<sub>4</sub> oriented along the {040} facet with enhanced activity for the sun-driven water oxidation. *Appl. Catal. B Environ.* **2016**, *180*, 630–636. [[CrossRef](#)]
31. Qiu, W.; Huang, Y.; Tang, S.; Ji, H.; Tong, Y. Thin-Layer Indium Oxide and Cobalt Oxyhydroxide Cobalt-Modified BiVO<sub>4</sub> Photoanode for Solar-Assisted Water Electrolysis. *J. Phys. Chem. C* **2017**, *121*, 17150–17159. [[CrossRef](#)]